Melting line and thermal equation of state of fcc-cobalt: A combined experimental and computational approach

Simone Anzellini, Silvia Boccato, Samuel Baty, Leonid Burakovsky, Daniele Antonangeli, Daniel Errandonea, Raffaella Torchio

Graphical Abstract

Melting line and thermal equation of state of fcc-cobalt: a combined experimental and computational approach

Simone Anzellini, Silvia Boccato, Samuel R. Baty, Leonid Burakovsky, Daniele Antonangeli, Daniel Errandonea, Raffaella Torchio

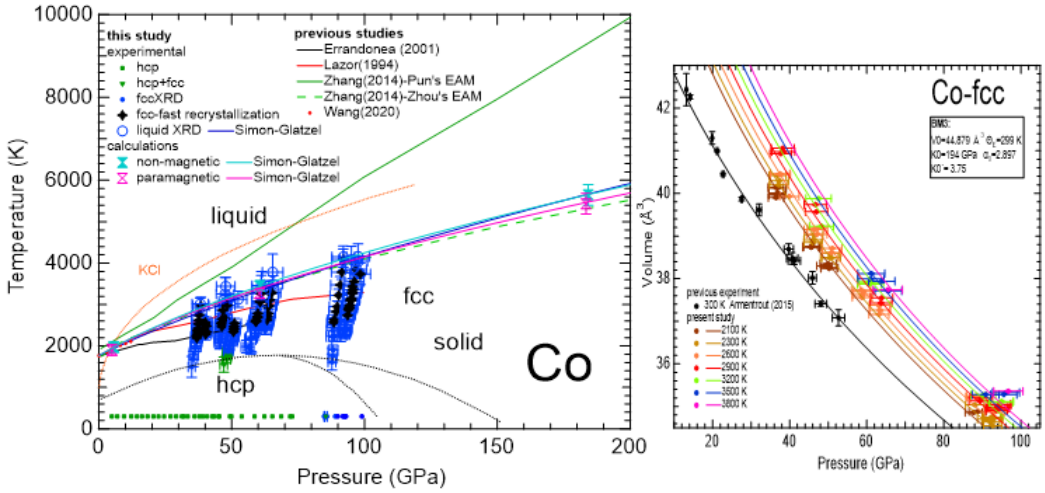

Melting line and thermal equation of state of fcc-cobalt: a combined experimental and computational approach

Simone Anzellini[a,b,*], Silvia Boccato[c], Samuel R. Baty[d], Leonid Burakovsky[d], Daniele Antonangeli[c], Daniel Errandonea[b], Raffaella Torchio[e]

[a] *Diamond Light Source Ltd., Harwell Science & Innovation Campus, Diamond House, Didcot, OX11 0DE, UK*
[b] *Departamento de Física Aplicada - Instituto de Ciencia de Materiales, Matter at High Pressure (MALTA) Consolider Team, Universidad de Valencia, Edificio de Investigacíon, C/Dr. Moliner 50, Burjassot, 46100 Valencia, ES*
[c] *Sorbonne Université, Muséum National d'Histoire Naturelle, UMR CNRS 7590, Insitut de Minéralogie, de Physique, des Matériaux, et de Cosmochinie, IMPMC, Paris, 75005, FR*
[d] *Los Alamos National Laboratory, P.O. Box 1663, Los Alamos, NM 87545, USA*
[e] *European Synchrotron Radiation Facility, 71 Avenue des Martyrs, Grenoble, CS 40220, 38043, FR*

Abstract

The melting line of cobalt has been investigated both experimentally, using synchrotron X-ray diffraction coupled with laser-heated diamond anvil cells, and theoretically, using *ab initio* simulations. Over the investigated pressure and temperature range - between 30 and 100 GPa and from ambient temperature up to 4000 K - the hexagonal close-packed structure, stable at ambient conditions, is replaced at high temperature by the face-centred cubic structure, observed stable till melting. The melting temperatures obtained by the two methods are in remarkable agreement and the melting line can be well described by a Simon-Glatzel equation of the form T_m=1768(K)(P(GPa)/35.62+1)$^{0.64}$. Finally, from the obtained results it was possible to determine a thermal equation of state for the cubic face-centred phase of Co.

Keywords: transition metals, melting curve, extreme condition, laser-heating, diamond anvil cell

*simone2.anzellini@uv.es

1. Introduction

Transition metals are characterized by a partially filled d-band and the consequent de-localization of their d-orbitals. This produces a strong metallic bonding responsible for a series of very interesting properties observed both in the pure transition metals and in their alloys. In particular, they are generally characterized by a high resistance to corrosion and wear, a good ductility and high yield strength, paramagnetism as well as high melting points and molar enthalpies of fusion. Concerning chemical reactivity, they can easily form alloys and metallic glasses. Due to all these properties, the technological applications and the economic importance of these elements, and their alloys, is immense (1; 2; 3; 4). As such, transition metals are among the most intensively studied family of elements, and in the past decades a big effort has been devoted to map and interpret systematic trends in their properties. Important examples include: the parabolic dependence of cohesive energy and bulk modulus on d-band filling (5), the sequence of most stable crystal structures associated with increasing band filling at ambient pressure (6), the pressure-induced increase of the d-band width going roughly as the fifth inverse power of the atomic volume (7) and the consequent pressure-induced suppression of ferromagnetism (8).
From a purely physical point of view, several studies have focused their attention to predict and understand the phase diagram of transition metals, shedding lights on the role of the pressure (P)-temperature (T)-induced filling of the d-shells into the observed structural and magnetic phase transitions. Several studies tried to unveil the thermodynamics and the microscopic processes of melting under pressure, given rise to many controversies among the different experimental and theoretical studies (9; 10; 11; 12).
Moreover, the study of transition metals under high pressure (HP) and high temperature (HT) is extremely relevant in geophysics and planetary science, as iron is the main constituent of terrestrial planetary cores (13). In particular, the characterization of the phase diagram and melting lines of iron (14; 15; 16; 17; 18; 19), iron-alloys (20; 21) and transition metals more in general (10; 22; 23) is of fundamental importance for understanding the composition, structure and dynamics of planetary cores (13; 24; 25; 26).

Among the transition metals, cobalt (Co), which is adjacent to iron (Fe) in the periodic table, has been suggested as analogue to iron when addressing Earth's core elastic anisotropy (27; 28). Furthermore, understanding the HP-HT-induced structural behavior of Co, can also shed light on the phase

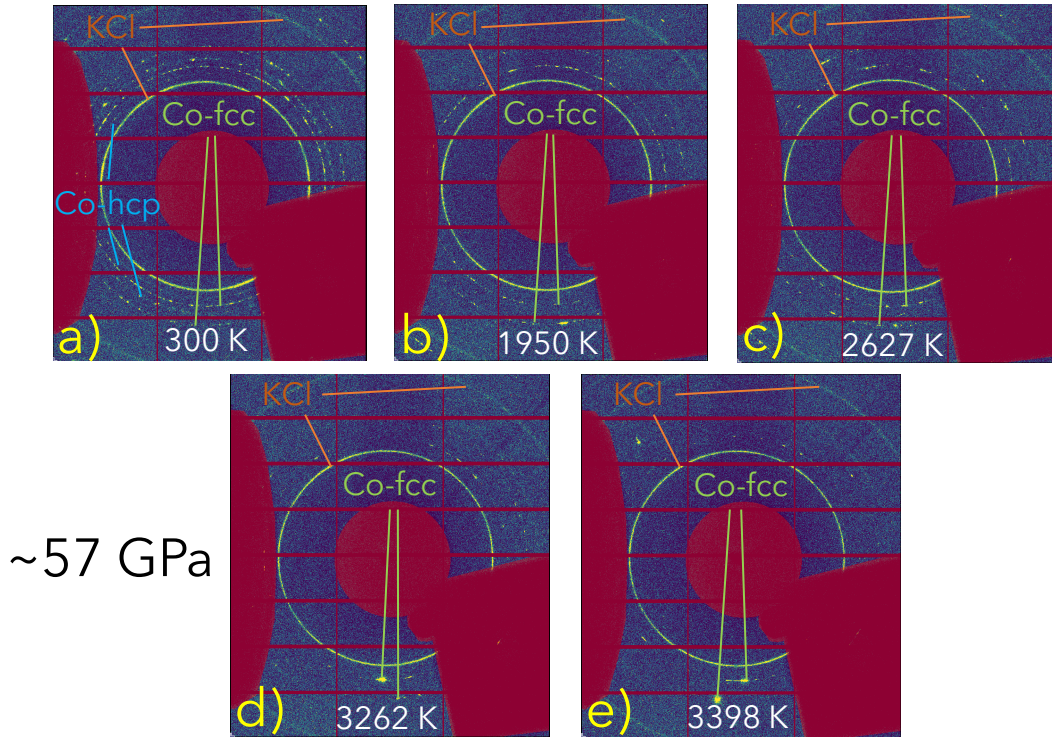

Figure 1: 2D XRD signal collected on the image plate of the Pilatus 2M detector showing snapshots of the T-induced textural evolution of the sample and the insulating material during a heating ramp performed around 57 GPa at 300 K, 1950 K, 2627 K, 3262 K, and 3398 K.

diagram of Fe in general. This includes the stability field of the γ phase of Fe with respect to the ϵ one and, the existence of cubic Fe-alloys under Earth's inner-core conditions (29; 30; 31). Therefore, several studies have focused their attention in characterizing Co structure, magnetism and elastic properties under extreme conditions (32; 33; 34; 35; 36; 37; 38; 39; 40; 41; 42).
At ambient conditions, cobalt is ferromagnetic and presents a hexagonal close-packed (hcp) structure. Upon compression, Co transforms to a face-centred cubic (fcc) phase in a P range between 70 and 150 GPa. This phase transition and the possible coexistence region of the two phases, has been shown to be strongly affected by the hydrostatic conditions of the experiments (30; 43). There is no measurable change of volume at the hcp-fcc transition but thereafter, the slope of the compression curve is reduced, in-

dicating a net increase of its elastic stiffness as a function of P (33).
A structurally similar phase transition is observed when increasing T up to 700 K at ambient P and this boundary has been measured to P above 70 GPa (44; 30). Within the fcc stability field, there is a T-induced-second-order phase transition from a ferromagnetic to a paramagnetic configuration. The thermal equation of state (EoS) of the fcc-Co was measured in a recent work by Armentout and Kavner (41) up to 57 GPa and 2400 K using a combination of laser-heated diamond anvil cell (LH-DAC) and X-ray diffraction (XRD).
As for other transition metals (*e.g.* Fe, Ta, Ni, etc..), the melting curve of Co reported in literature presents several discrepancies between the various studies. Early experiments performed by both Errandonea *et al.* (10) and Lazor (45) in LH-DAC, using the direct observation of movements on the sample surface as melting criterion (speckle technique), resulted in melting curves that differ by 400 K at 60 GPa. A more recent experiment was performed by Wang *et al.* (46), but only up to 12 GPa, in a high volume cubic press using as melting criterion both the plateaus in the T vs. laser power dependence and *ex situ* scanning electron microscope (SEM) analysis of the texture of the recovered sample. When extrapolated to higher P, the obtained results seem to be more in agreement with the melting line reported by Lazor (45). In contrast, previous resistivity measurements performed by Ezenwa and Secco (47) are more in line with the results obtained by Errandonea *et al.*(10). Noteworthy, *in situ* investigation by synchrotron techniques have not been performed yet.

From a computational point of view, the melting line of Co was calculated by Zhang *et al.* (29) using molecular dynamics (MD) simulations with the two embedded atoms method (EAM) potentials. However, the melting line obtained with these simulations plots significantly higher than the experimental determinations.

Since the early melting experiment of Errandonea *et al.* (10), LH-DAC technology has considerably progressed, as *in situ* melting diagnostics. In particular, LH-DAC combined with synchrotron XRD, it has now become a challenging but routinely used technique for *in situ* characterizations of phase diagrams and melting lines of samples at P up to 3 Mbar and T in excess of 5000 K (48; 49). Indeed, it allows reliable analysis of the P-T-induced chemical, textural and structural evolution of both the sample and the insulating material, to be performed in a relatively short time (few seconds) compatible

with confinement of liquid within the experimental chamber. In addition, XRD technique provides an objective melting criterion, *i.e.* the appearance of a diffuse signal in the diffraction pattern due to the scattering from the liquid sample (unlike crystalline materials, liquids and amorphous materials do not have a long range order, resulting in the absence of relatively sharp diffraction peaks, replaced by a diffuse signal). Thanks to the advances in this technique (metrology included) several discrepancies previously observed on the melting curves of other transition metals have been solved (50).
For these reasons, we decided to study the phase diagram and melting curve of Co both experimentally, using LH-DAC combined with XRD, and theoretically, using *ab initio* calculations based on the density functional theory (DFT).

2. Methods

2.1. Experiments

Three membrane DACs with culet sizes ranging from 300 μm down to 150 μm were equipped with pre-indented and laser-drilled rhenium gaskets. The sample was cut from a 4 μm thick 99.95 % Co policrystalline deposition prepared by Eric Monsifrot from the SARL DEPHIS in Etupes (FR). The obtained samples were sandwiched between two KCl disks previously-prepared by fs laser micro-machining and loaded in the high pressure chamber of the DAC. The KCl disks were used as insulating material as well as pressure transmitting medium (PTM) and gauge. In order to minimize any chemical reaction, the KCl disks were oven dried at 150 °C (above the KCl dehydration T) for four hours before being used for the loading. For the same reason, the loaded cells were placed (slightly opened), back in the oven while waiting to be used on the beamline.
The experiment was performed at the extreme conditions beamline I15 at Diamond Light Source (51). The beamline's polychromatic beam was tuned to 29.5 keV and focused down to 9×6 μm (Full Width at Half Maximum -FWHM) using two pairs of KB-mirrors. A Si Pilatus 2M detector was used to rapidly collect diffraction data from the sample while keeping a good signal-to-noise ratio. The sample-to-detector distance was determined from the diffraction rings of a CeO_2 standard using the calibration routine of the DIOPTAS software suite (52).
The HP-HT experiment was performed using the laser-heating system mounted

on the beamline and following the procedure described in Anzellini and Boccato (48). Before each heating ramp, the sample was brought to the target P evaluated according to the KCl equation of state following the calibration of Dewaele *et al.* (53). Two 100 W Nd:YAG lasers were used to heat the sample from each side minimizing the axial thermal gradients. Both lasers were individually focused on the sample until clear hot spots of similar temperatures were obtained. The lasers were then intentionally unfocused and spatially coupled in order to maximize the surface at constant T on both sample sides ($\sim$ 40 μm in diameter, much larger than the X-ray beam size). T was measured from each side simultaneously via spectral radiometry (Planck fitting in the range between 450 nm and 950 nm) and the final T was assumed as the average of the two determinations. The maximum difference in T measured on the two sides of the sample and the standard deviation of the histograms obtained from their two-colours pyrometry (Benedetti and Loubeyre (54)) was used as the error in the measurement. The corresponding thermal P was obtained from the thermal EoS of Dewaele *et al.* (53) under the assumption that both Co and KCl were experiencing the same T. Considering the present sample geometry and the corresponding axial thermal gradient, the maximum error in P was calculated as half the difference between the pressure obtained from the KCl at the measured T (surface of contact with the Co) and the one from the KCl at ambient T (when in contact with the diamond). Before and after each heating ramp, the alignment between the X-rays, the lasers and the T reading spot was checked following the procedure described in Anzellini *et al.* (51).

The heating ramps were performed in "trigger mode": both lasers were set to a target power; after 0.3 s a diffraction pattern and a T measurement were simultaneously collected; 0.3 s after the XRD collection, the power of both lasers was set back to zero. This procedure, while assuring T stabilization and sample equilibration, allowed us to minimize the interaction time between the laser and the sample, so reducing the risk of possible chemical reactions, and to perform any adjustment in the optics when needed. During each heating ramp, the lasers powers were increased until a diffuse signal was detected in the diffraction pattern or it was not possible to further increase T (changes in the insulating conditions of the sample). Several heating ramps were performed on the same samples at different P–T conditions, each time on a different region, and suitability of the measurements (unreacted sample, good ratio in the sample vs. KCl signal etc.) were assessed by collecting XRD patterns before the actual ramp.

During the data analysis, great care was taken to investigate the different aspects of the experiment. The reliability of T measurements was double checked following the procedure described in Benedetti and Loubeyre (54). An accurate analysis of the diffraction patterns was performed to detect the onset of melting and to obtain structural and textural information about the sample and the insulating material. Masks were applied on a per-image basis and the images azimuthally integrated using the DIOPTAS suite (52). Both Co and KCl data were treated as powder data and a Pawley analysis was performed with the TOPAS suite (55) using previously reported parameters as starting values. Finally, the outcome of the analysis of the *in situ* XRD measurements were associated to the corresponding T, so to obtain a precise structural evolution of the sample as a function of P and T.

2.2. Calculations

Theoretical calculations were performed based on a DFT approach, with the projector-augmented-wave (PAW) (56) implementation and the generalized gradient approximation (GGA) for exchange-correlation energy, in the form known as Perdew-Burke-Ernzerhof (PBE) (57). For these calculations the Vienna *Ab initio* Simulation Package (VASP) was used. GGA was preferred to local density approximation (LDA), because, in spite of the case of hcp-Co, where LDA calculations yields to single crystalline elastic moduli in closer agreement with experimental results than GGA calculations (27), GGA well account for the compressibility curve (37). Furthermore, it is known that LDA does not accurately describe the properties of other $3d$ transition metals *e.g.* chromium for which its predictions are in drastic disagreement with experiment (58; 59), and iron for which it produces a wrong ground state (60; 61; 62; 63). LDA also fails in assessing the strength of the magnetovolume effect. On the other hand, GGA correctly predicts the structural and magnetic phase diagrams (64).

Co was modeled using the core-valence representation $[^{12}\mathrm{Mg}]3p^6 3d^7 4s^2$, *i.e.*, the 15 outermost electrons were assigned to the valence. The valence electrons were represented with a plane-wave basis set with a cutoff energy of 340 eV, while the core electrons were represented by PAW pseudopotential. The present *ab initio* Quantum Molecular Dynamics (QMD) simulations of the melting curves of both the non magnetic (NM) fcc-Co and the paramagnetic (PM) fcc-Co were carried out using the Z method implemented within VASP (65). The simulations were carried out with a single Γ-point; with such a large supercell, full energy convergence, to ~ 10 meV/atom was

achieved in every case considered, which is equivalent to an error of $\sim$ 100 K in the value of the melting temperature (T_m), within the accuracy of the Z method itself.

For the calculations on PM fcc-Co, the GGA+U scheme with spin-orbit coupling developed for the calculation of the properties of paramagnetic materials (66) was applied. Specifically, the Dudarev approach (67), in which only the difference U-J is meaningful rather than the values of the two parameters separately, was used. An U-J=5.0 eV was chosen following Aryasetiawan *et al.* (68). Note that the melting curve of PM fcc-Co does not seem to depend on the choice of the numerical value of U-J. Several melting points of PM fcc-Co were calculated using U-J in the 2.5-7.5 eV range. Although the corresponding values of P and T are slightly different from those of PM fcc-Co with U-J=5.0 eV having the same densities, all of the computed melting points lie on the melting curve of PM fcc-Co with U-J=5.0 eV. Thus, the melting curve of PM fcc-Co is essentially unique. Note that U-J=0 corresponds to the case of NM fcc-Co; even in this case the two melting curves are virtually identical in a very wide P range; their difference starts manifesting itself at $\rho \sim 14.5$ g/cm^3 (a pressure of $\sim$ 500 GPa) and $T_m \sim 9000$ K.

3. Results and discussion

3.1. Phase diagram

Ten HT ramps were performed at selected P following the procedure described in the method section. The data were collected in a P-T range between 15 GPa and 98 GPa and from ambient T up to 4200 K. In this investigated range it was possible to index Co hcp and fcc solid phases and the B2 phase of KCl (used as PTM and standard). Only the ramp performed around 40 GPa showed some formation of CoO(69) above 2600 K, therefore the data obtained in this run above this T were discarded. The analysis of XRD patterns also excludes the formation of cobalt carbide and dicobalt carbide (70), thus if any reaction occurred, the amount of unwanted phases is below the detection limits of the XRD technique.

An overall similar T-induced textural evolution was observed in each of the performed ramps (Fig. 1). At ambient T (Fig. 1a) Co shows a $fcc-hcp$ coexistence[1], with both phases presenting the texture of a highly oriented

[1]The observed fcc-hcp coexistence is a consequence of the alignment of the two lasers

powder. Conversely, KCl in the B2 phase shows a nice powder signal. Upon T increase, the signal from the KCl PTM does not change considerably. On the other hand, it is possible to follow the progressive grain growth of Co, starting right after its complete transformation to the fcc structure as evidenced by the evolution from a powder-like (characterized by the presence of rings) to a single-crystal-like (spots) XRD pattern. Similarly to the case of other transition metals (14; 22; 71), above a certain T it was possible to observe the phenomenon referred to as "fast re-crystallization" *i.e.* for each measurement, single crystal spots belonging to the same crystallographic planes, disappear and appear at different azimuthal angles on the image plate (Fig.1d and Fig.1e) due to grain growth and re-orientation. Finally, under further T-increase, in eight of the performed ramps, it was possible to observe the appearance of a diffuse halo, characteristic of a liquid sample (Fig.2a). The coexistence of liquid and solid phases for a single component system is a direct consequence of the presence of thermal gradients. Specifically, axial thermal gradients lead to XRD patterns simultaneously showing the liquid signal from the hotter portion of the sample at the surfaces and solid signal from the colder inner-most part of the sample. With further increase of T above melting, the relative intensity of the diffuse signal vs. the solid diffraction peaks increases as inner parts of the sample melt.

Changes in T vs. laser power plot, such as T plateau or sudden drops are often used as additional melting criterion. However, similar to the results obtained for Fe with an identical technique (14), only few of the experimental ramps of the present experiment evidenced such a behavior in the T evolution. On the other hand, as shown in Fig.2b, it was possible to observe a plateau in the volumetric thermal expansion of fcc-Co at T corresponding to the estimated melting. Such phenomenon, arising from the inevitable thermal gradient within the sample can be interpreted as an additional confirmation of its melting. Indeed, fcc-Co volume expands with increasing T as commonly expected for solids up to a threshold value, corresponding to melting. The solid signal observed at higher temperatures is coming from un-melted portions of the samples that, due to thermal gradients, are still below melting T, with a volume effectively pinned at that of the hottest solid

on the opposite surfaces of the samples and the successive rapid quench performed before the beginning of the actual heating ramp

before melting (72).

Due to the observed thermal gradients and the sensitivity of the XRD technique to the signal from liquid sample, the melting T was assumed as the average between the T of the last pattern corresponding to a completely solid sample and the first one showing diffuse scattering from a liquid.

The Co phase diagram constructed on the basis of the present experiments is reported in Fig.3 and compared with results from our calculations and from literature. The ambient T data are those obtained before each heating ramps and do not necessarily represent the thermodynamic equilibrium (as some point are obtained from cold compression and others from the sample quenched from HT). We note however that the observed fcc-hcp transition pressure at 300 K is in agreement with those obtained from non-hydrostatic compression (73), and lower than what expected on the basis of quasi-hydrostatic data (30; 37). We also note a good agreement between the HP-HT stability of the fcc phase observed in this study and the fcc-hcp phase boundary reported in previous studies(30). However, because of the minimal temperatures that can be generated and measured in LH-DAC experiments it was only possible to obtain an *in situ* characterization of the HP-HT fcc-hcp phase boundary of Co for the ramp around 47 GPa.

The melting curve established on the basis of the here-obtained melting points can be well described by a Simon-Glatzel equation with the following parameters:

$$Tm = 1768.15(K)(P(GPa)/35.62 + 1)^{0.64} \quad (1)$$

Extrapolation of the present experimental melting curve to lower pressure, down to ambient P is in remarkable agreement with the data recently obtained in large volume press by Wang *et al.* (46). On the contrary, the present melting curve is higher than early determination by direct observation of movement on the sample surface(45; 10). In particular, at 60 GPa the differences are of the order of 800 K and 400 K with respect to the melting line of Errandonea (10) and Lazor (45), respectively. A discrepancy between the melting line obtained using these two different melting criterion is not surprising as, with only few exceptions (74; 75; 71), similar situations were observed in most of the melting studies reported in the literature (14; 22; 76; 11; 77). However, it is interesting to note that the

melting line reported by Errandonea (10) corresponds to the onset of fast recrystallization (Fig.3) as already the case for Fe, for which the melting curve determined by the speckle method(15) plots very close to the onset of fast crystallization (14). Such a correlation is not accidental, and is likely inherent to technical aspects of the LH-DAC and speckle techniques. In fact, grain reorientation and grain growth can facilitate grain migration under thermal gradients, which can be perceived by the speckle technique as movements on the sample surfaces and mis-interpreted as formation of liquid. On the other hand, it is more difficult to explain the discrepancy observed with respect to the data obtained by Lazor (45) that have been obtained using the same speckle technique as in Errandonea (10). Possibly these differences should be ascribed to differences in the adopted P-T metrology.

Concerning the comparison with calculations, our experimental and computational results are in good agreement. Computed melting curve is also in good agreement with the results of Zhang *et al.* (29) obtained using MD with a Zhou´s potential, whereas it is much lower than the one obtained by the same group using MD with a Pun potential (29), with a difference as large as 1900 K at 100 GPa.

3.2. Thermal equation of state

Fig. 4 shows the volumes measured for fcc-Co at HP-HT and the resulting compression curves along different isotherms. Starting from the presented data it was possible to establish the P-V-T equation of state (EoS) for fcc-Co using the EOSfit software suite (78). According to the formalism described in Angel *et al.* (78) P at HT can be described as the sum of P at a reference T condition (typically 300 K) and the thermal P with increasing T evaluated along isochors, and hence it can be expressed as:

$$P(V,T) = P(V,300K) + P_{Th}(T) \tag{2}$$

where the $P(V$, 300 K) is the isothermal EoS of the material at ambient T and $P_{Th}(T)$ the thermal pressure. In the present work, $P(V$, 300 K) was calculated from the data reported by Armentrout and Kavner (41), while (P_{Th}) was modelled fallowing Holland and Powell:

$$P_{Th}(T) = \alpha_0 K_0 \frac{\Theta_E}{\zeta_0}\left(\frac{1}{exp(\Theta_E/T)-1} - \frac{1}{exp(\Theta_E/300)-1}\right) \tag{3}$$

Table 1: The eight *ab initio* melting points of PM *fcc*-Co, (P_m, $T_m \pm \Delta T_m$), obtained from the Z method implemented with VASP.

lattice constant (Å)	density (g/cm^3)	P_m (GPa)	T_m (K)	ΔT_m (K)
3.6	8.3901	4.96	1900	125.0
3.4	9.9595	60.5	3270	125.0
3.3	10.893	99.9	4150	250.0
3.2	11.946	183.4	5430	250.0
3.1	13.140	290.6	6850	250.0
3.0	14.498	448.4	8570	375.0
2.9	16.050	681.7	10610	375.0
2.8	17.832	1030	13040	500.0

Where Θ_E is the Einstein T of the material (299 K for Co), K_0 is the bulk modulus obtained from the isothermal EoS at ambient T, α_0 is the thermal expansion coefficient at 300 K and ζ_0 is expressed as:

$$\zeta_0 = \frac{(\Theta_E/300)^2 exp(\Theta_E/300)}{(exp(\Theta_E/300) - 1)^2} \tag{4}$$

As shown in Fig.4 data grouped considering T ranges of $\pm$ 100 K are well described by a 3^{rd} order Birch-Murnaghan EoS at ambient T and a thermal pressure modelled according Holland and Powell expression with the following parameters: V_0=44.88(5) Å^3; K_0=194(2) GPa; K_0^I=3.75(3) and α_0=2.897(8)$\times 10^{-5}$ K^{-1}.

3.3. Calculations

The results of the present QMD melting simulations obtained using VASP are summarized in Tables 1 and 2 and compared to experimental results and work in literature in Fig. 3. The errors in the obtained melting points (T_m) are half of the increment of the initial T for a series of computer runs at the corresponding density (65). Increment of 250 K were chosen for the first two points, and increased at higher pressures (500 K for the 3rd, 4th and 5th pressure point, 750 K for the 6th and 7th pressure point, and 1000 K for the last (8th) pressure point. The corresponding T_m errors are listed in the two tables as ΔT_m. The errors in melting P (P_m) are negligibly small, of order 1-2 GPa for each case.

The best fits to the corresponding six data points to a Simon-Glatzel

Table 2: The eight *ab initio* melting points of NM fcc-Co, (P_m, $T_m \pm \Delta T_m$), obtained from the Z method implemented with VASP.

lattice constant (Å)	density (g/cm^3)	P_m (GPa)	T_m (K)	ΔT_m (K)
3.6	8.3901	5.60	1970	125.0
3.4	9.9595	60.6	3450	125.0
3.3	10.893	100.0	4250	250.0
3.2	11.946	184.2	5650	250.0
3.1	13.140	294.9	7170	250.0
3.0	14.498	460.8	9050	375.0
2.9	16.050	710.3	11400	375.0
2.8	17.832	1088	14380	500.0

equation provide, respectively for paramagnetic and non magnetic calculations, the following melting curves:

$$T_m^{\mathrm{PM\,fcc-Co}}(P) = 1768 \left(1 + \frac{P}{25.9}\right)^{0.54}, \tag{5}$$

and

$$T_m^{\mathrm{NM\,fcc-Co}}(P) = 1768 \left(1 + \frac{P}{26.4}\right)^{0.56}. \tag{6}$$

Data are very little dispersed, with fits yielding to χ^2 of ≈ 1.5 if T_m at ambient P is fixed to the experimentally determined value of 1768 K. Otherwise χ^2 values are around 1, if T_m at ambient P is left as a free parameter. In this latter case best fit values for T_m are 1762.4 K for PM fcc-Co and 1768.1 K for NM fcc-Co, this second in closer agreement with experiments at ambient pressure.

The initial slopes ($dT_m(P)/dP|_{P=0}$) of the two melting curves are 36.9 K/GPa (PM) and 37.5 K/GPa (NM). Either value is consistent with (37.1±1.1) K/GPa given by the Clausius-Clapeyron relation $dT_m/dP = T_m\,\Delta V_m/\Delta H_m$, where ΔV_m and ΔH_m are the volume and enthalpy changes at melt, respectively, with the literature values of $\Delta V_m = 0.35$ cm^3/mole and $\Delta H_m = 16.7 \pm 0.5$ kJ/mole. The present experimental and simulated Simon-Glatzel melting curves (represented in Fig. 3 with blue, cyan and pink continuous lines, respectively) are in mutual agreement. A closer look indicates that melting of the simulated PM phase of Co is in sightly better agreement with experimental determination up to about 110 GPa, while, at higher pressures,

NM calculations yields to a better agreement with the extrapolation of the measured melting curve.

4. Conclusions

The P–T phase diagram of cobalt was determined up to 100 GPa and 4000 K by LH-DAC and synchrotron-based XRD measurements. QMD simulation for both non magnetic and paramagnetic phases of fcc-Co were also performed up to 1 TPa and 14000 K to characterize its melting curve. The agreement between the experiment and the calculation is excellent in the P-T range experimentally explored, with the computed melting for the paramagnetic phase in slightly better agreement with the experimental data. Unit-cell volumes of the fcc phase measured at high pressures and high temperatures were used to obtain the thermal equation of state of fcc-Co. Data can be well fit by a combination of a 3rd order Birch-Murnaghan EoS describing the $P-V$ compression curve at ambient T with a Holland and Powell expression for the thermal pressure with the following parameters: V_0=44.88(5) $Å^3$; K_0=194(2) GPa; K_0^I=3.75(3) and α_0=2.897(8)$\times 10^{-5}$ K^{-1}. Finally, the value of 37.5 K/GPa of the slope of Co melting line at 0 GPa obtained from the calculations performed for NM-fcc Co can be compare to the values reported for Fe (30.5 K/GPa, (14)) and Ni (38 K/GPa, (22)). Although, we note an increase in the values of the melting slope as a function of the d electron occupation, this increase is relatively small and can be considered within the experimental error. Therefore, the obtained results do not necessarily support the hypothesis that the behavior of the melting curve of $3d$ transition metals depends on the d-electron occupation as proposed in Japel *et al.* (12).

Acknowledgement(s)

The authors acknowledge the DLS synchrotron facility for provision of beamtime at the beamlines I15 (exp. CY21943). The authors are also grateful to Francesca Miozzi, Ruggero Giampaoli, Annette Kleppe and Allan Ross for their support in the experimental preparation. Femtosecond laser micro-machining at IMPMC has been developed and realized by the "Cellule Project" with the financial support of ANR 2010-JCJC-604-01. D.A. and S.B. have received funding from the European Research Council (ERC) under the European Union's Horizon 2020 research and innovation

programme (Grant agreement No. 724690). This work was supported by the Generalitat Valenciana under grants PROMETEO CIPROM/2021/075-GREENMAT and MFA/2022/007, and by the Spanish Ministerio de Ciencia e Innovación, Agencia Estatal de Investigación, and the European Union (MCIN/AEI/10.13039/501100011033) under grants PID2019–106383GB-41 and RED2018–102612-T (MALTA Consolider Team).This study forms part of the Advanced Materials program and is supported by MCIN with funding from European Union Next Generation EU (PRTR-C17.I1) and by the Generalitat Valenciana. S.A. thanks the Generalitat Valenciana for the CIDEGENT grant no. CIDEXG/2022/6.

Disclosure statement

The authors declare no conflict of interest

Data Availability

The datasets generated during and/or analysed during the current study are available from the corresponding author upon request.

Notes on contributor(s)

S.B. and R.T. conceived the experiment. S.A., S.B and R.T. conducted the HP-HT experiment. S.A. analyzed the results. L.B. and S.R.B. performed the calculations. D.E. and D.A contributed to the discussion and provided funding. The manuscript was written through contributions of all authors. All authors have given approval to the final version of the manuscript.

References

[1] W. Wang, C. Dong, C. Shek, Bulk metallic glasses, Materials Science and Engineering: R: Reports 44 (2-3) (2004) 45–89. doi:10.1016/j.mser.2004.03.001.

[2] A. T. Motta, A. Yilmazbayhan, M. J. G. da Silva, R. J. Comstock, G. S. Was, J. T. Busby, E. Gartner, Q. Peng, Y. H. Jeong, J. Y. Park, Zirconium alloys for supercritical water reactor applications: Challenges and possibilities, Journal of Nuclear Materials 371 (1-3) (2007) 61–75. doi:10.1016/j.jnucmat.2007.05.022.

[3] X. LIU, P. CHU, C. DING, Surface modification of titanium, titanium alloys, and related materials for biomedical applications, Materials Science and Engineering: R: Reports 47 (3-4) (2004) 49–121. doi:10.1016/j.mser.2004.11.001.

[4] C. Suryanarayana, Mechanical alloying and milling, 2001.

[5] J. Friedel, The Physics of Metals, Cambridge University Press, 1991.

[6] D. Pettifor, Theory of the crystal structures of transition metals, J. Phys. C: Solid State Phys 3 (1970) 367.

[7] V. Heine, s-d interaction in transition metals*, Physical Review 153 (1967) 673.

[8] R. Torchio, O. Mathon, S. Pascarelli, XAS and XMCD spectroscopies to study matter at high pressure: Probing the correlation between structure and magnetism in the 3d metals, Coordination Chemistry Reviews 277-278 (2014) 80–94. doi:10.1016/j.ccr.2014.02.024.

[9] A. Landa, P. Söderlind, A. V. Ruban, O. E. Peil, L. Vitos, Stability in bcc transition metals: Madelung and band-energy effects due to alloying, Physical Review Letters 103 (23) (2009) 235501. doi:10.1103/physrevlett.103.235501.

[10] D. Errandonea, B. Schwager, R. Ditz, C. Gessmann, R. Boehler, M. Ross, Systematics of transition-metal melting, Physical Review B 63 (13) (2001) 132104.
URL `http://link.aps.org/doi/10.1103/PhysRevB.63.132104`

[11] R. Hrubiak, Y. Meng, G. Shen, Microstructures define melting of molybdenum at high pressure, Nature Communications 8 (2017) 14562.

[12] S. Japel, B. Schwager, R. Boehler, M. Ross, Melting of copper and nickel at high pressure: The role of d electrons, Physical Review Letters 95 (16) (2005) 1–4.

[13] J.-P. Poirier, Introduction to the Physics of the Earth's Interior, Cambridge University Press, 2003.

[14] S. Anzellini, A. Dewaele, M. Mezouar, P. Loubeyre, G. Morard, Melting of iron at Earth's inner core boundary based on fast X-ray diffraction., Science 340 (6131) (2013) 464–6.

[15] R. Boehler, Temperatures in the Earth's core from melting-point measurements of iron at high static pressures, Nature 363 (6429) (1993) 534–536.

[16] G. Aquilanti, A. Trapananti, A. Karandikar, I. Kantor, C. Marini, O. Mathon, S. Pascarelli, R. Boehler, Melting of iron determined by X-ray absorption spectroscopy to 100 GPa, Proceedings of the National Academy of Sciences 112 (39) (2015) 12042–12045.

[17] G. Morard, S. Boccato, A. Rosa, S. Anzellini, F. Miozzi, L. Henry, G. Garbarino, M. Mezouar, M. Harmand, F. Guyot, E. Boulard, I. Kantor, T. Irifune, R. Torchio, Solving controversies on the iron phase diagram under high pressure, Geophysical Research Letters 45 (2018) 11, 074 – 11, 082.

[18] R. Sinmyo, K. Hirose, Y. Ohishi, Melting curve of iron to 290 gpa determined in a resistance-heated diamond-anvil cell, Earth and Planetary Science Letters 510 (2019) 45.

[19] J. M. Jackson, W. Sturhahn, M. Lerche, J. Zhao, T. S. Toellner, E. E. Alp, S. V. Sinogeikin, J. D. Bass, C. A. Murphy, J. K. Wicks, Melting of compressed iron by monitoring atomic dynamics, Earth and Planetary Science Letters 362 (2013) 143–150. doi:10.1016/j.epsl.2012.11.048.

[20] G. Morard, D. Andrault, N. Guignot, J. Siebert, G. Garbarino, D. Antonangeli, Melting of Fe Ni Si and Fe Ni S alloys at megabar pressures : implications for the core mantle boundary temperature, Phys Chem Minerals 38 (2011) 767–776. doi:10.1007/s00269-011-0449-9.

[21] S. Boccato, R. Torchio, S. Anzellini, E. Boulard, F. Guyot, T. Irifune, M. Harmand, I. Kantor, F. Miozzi, P. Parisiades, A. D. Rosa, D. Antonangeli, G. Morard, Melting properties by x-ray absorption spectroscopy: common signatures in binary fe–c, fe–o, fe–s and fe–si systems, Scientific Reports 10 (2020) 11663. doi:.org/10.1038/s41598-020-68244-3.

[22] O. Lord, I. Wood, D. Dobson, L. Vocadlo, W. Wang, A. Thomson, E. Wann, G. Morard, M. Mezouar, M. Walter, The melting curve of Ni to 1 Mbar, Earth and Planetary Science Letters 408 (2014) 226–236.

[23] S. Boccato, R. Torchio, I. Kantor, G. Morard, S. Anzellini, R. Giampaoli, R. Briggs, A. Smareglia, T. Irifune, S. Pascarelli, The Melting Curve of Nickel Up to 100 GPa Explored by XAS, Journal of Geophysical Research: Solid Earth 122 (2017) 1–10.

[24] G. Morard, D. Andrault, D. Antonangeli, Y. Nakajima, A. Auzende, E. Boulard, S. Cervera, A. Clark, O. Lord, J. Siebert, V. Svitlyk, G. Garbarino, M. Mezouar, Fe-FeO and Fe-Fe3C melting relations at Earth's core-mantle boundary conditions: Implications for a volatile-rich or oxygen-rich core, Earth and Planetary Science Letters 473 (2017) 94–103.

[25] K. Hirose, B. Wood, L. Vocadlo, Light elements in the earth´s core, Nature Reviews Earth & Environment 2 (2021) 645–658.

[26] F. Miozzi, G. Morard, D. Antonangeli, M. Baron, S. Boccato, A. Pakhomova, G. Garbarino, M. Mezouar, G. Fiquet, Eutectic melting of fe-3 at% si-4 at% c up to 200 GPa and implications for the earth's core, Earth and Planetary Science Letters 544 (2020) 116382. doi:10.1016/j.epsl.2020.116382.

[27] D. Antonangeli, M. Krisch, G. Fiquet, D. L. Farber, C. M. Aracne, J. Badro, F. Occelli, , H. R. . G. Cedex, France, Elasticity of cobalt at high pressure studied by inelastic x-ray scattering", d. antonangel, Physical Review Letters 93 (2004) 215505.

[28] D. Antonangeli, S. Merkel, D. L. Farber, Elastic anisotropy in hcp metals at high pressure and the sound wave anisotropy of the earth´s inner core, Geophysical Research Letters 33 (2006) L24303. doi:10.1029/2006GL028237.

[29] W. J. Zhang, Y. F. Peng, Z. L. Liu, Molecular dynamics study of melting curve, entropy of fusion and solid-liquid interfacial energy of cobalt under pressure, Physica B: Condensed Matter 440 (2014) 33–40.

[30] C. S. Yoo, H. Cynn, P. Söderlind, V. Iota, New b (fcc) -Cobalt to 210 GPa, Physical Review Letters 84 (18) (2000) 4132–4135.

[31] A. B. Belonoshko, S. I. Simak, W. Olovsson, O. Y. Vekilova, Elastic properties of body-centered cubic iron in earth's inner core, Physical Review B 105 (18) (2022) l180102. doi:10.1103/physrevb.105.l180102.

[32] A. Dewaele, M. Torrent, P. Loubeyre, M. Mezouar, Compression curves of transition metals in the mbar range: Experiments and projector augmented-wave calculations, Physical Review B - Condensed Matter and Materials Physics 78 (10) (2008) 1–13.

[33] A. F. Goncharov, J. Crowhurst, J. M. Zaug, Elastic and vibrational properties of cobalt to 120 GPa, Physical Review Letters 92 (11) (2004) 115502. doi:10.1103/physrevlett.92.115502.

[34] H. Fujihisa, K. Takemura, Equation of state of cobalt up to 79 gpa, 1996.

[35] B. Strauss, F. Frey, W. Petry, J. Trampenau, K. Nicolaus, S. Shapiro, J. Bossy, Martensitic phase transformation and lattice dynamics of fcc cobalt, 1996.

[36] J. Gump, H. Xia, M. Chirita, R. Sooryakumar, M. A. Tomaz, G. R. Harp, Elastic constants of face-centered-cubic cobalt, Journal of Applied Physics 86 (11) (1999) 6005–6009. doi:10.1063/1.371647.

[37] D. Antonangeli, L. R. Benedetti, D. L. Farber, G. Steinle-Neumann, A. L. Auzende, J. Badro, M. Hanfland, M. Krisch, Anomalous pressure evolution of the axial ratio ca in hcp cobalt: Interplay between structure, magnetism, and lattice dynamics, Applied Physics Letters 92 (11) (2008) 10–13.

[38] D. Antonangeli, M. Krisch, G. Fiquet, J. Badro, D. L. Farber, A. Bossak, S. Merkel, Aggregate and single-crystalline elasticity of hcp cobalt at high pressure, Physical Review B 72 (13) (2005) 134303. doi:10.1103/physrevb.72.134303.

[39] J. C. Crowhurst, D. Antonangeli, J. M. Brown, A. F. Goncharov, D. L. Farber, C. M. Aracne, Determination of the high pressure elasticity of cobalt from measured interfacial acoustic wave velocities, Applied Physics Letters 89 (11) (2006) 111920. doi:10.1063/1.2220537.

[40] V. A. de la Peña O'Shea, I. de P. R. Moreira, A. Roldán, F. Illas, Electronic and magnetic structure of bulk cobalt: The α, β, and ϵ-phases from density functional theory calculations, The Journal of Chemical Physics 133 (2) (2010) 024701. doi:10.1063/1.3458691.

[41] M. M. Armentrout, A. Kavner, A new high pressure and temperature equation of state of fcc cobalt, Journal of Applied Physics 118 (19) (2015).

[42] S. Boccato, R. Torchio, P. D'Angelo, A. Trapananti, I. Kantor, V. Recoules, S. Anzellini, G. Morard, T. Irifune, S. Pascarelli, Compression of liquid Ni and Co under extreme conditions explored by x-ray absorption spectroscopy, Physical Review B 100 (18) (2019) 180101. doi:10.1103/PhysRevB.100.180101.

[43] R. Torchio, C. Marini, Y. Kvashnin, I. Kantor, O. Mathon, G. Garbarino, C. Meneghini, S. Anzellini, F. Occelli, P. Bruno, A. Dewaele, S. Pascarelli, Structure and magnetism of cobalt at high pressure and low temperature, Physical Review B 94 (2016) 024429.

[44] C.-S. Yoo, P. Söderlind, H. Cynn, The phase diagram of cobalt at high pressure and temperature: the stability of -cobalt and new -cobalt, Journal of Physics: Condensed Matter 10 (20) (1998) L311–L318.

[45] P. Lazor, Phase diagrams, elasticity and thermodynamics of ni, co and fe under high pressure, Ph.D. thesis, Faculty of Science and Technology (1994).

[46] J. Wang, D. He, X. Li, J. Zhang, Q. Li, Z. Wang, Y. Su, Y. Tian, J. Yang, B. Peng, The melting curve of cobalt under high pressure, Solid State Communications 307 (2020) 113805.

[47] I. C. Ezenwa, R. A. Secco, Invariant electrical resistivity of co along the melting boundary, Earth and Planetary Science Letters 474 (2017) 120–127. doi:10.1016/j.epsl.2017.06.032.

[48] S. Anzellini, S. Boccato, A practical review of the laser-heated diamond anvil cell for university laboratories and synchrotron applications, Crystals 10 (2020) 459.

[49] S. Tateno, Y. Kuwayama, K. Hirose, Y. Ohishi, The structure of Fe-Si alloy in Earth's inner core, Earth and Planetary Science Letters 418 (2015) 11–19.

[50] P. Parisiades, A Review of the Melting Curves of Transition Metals at High Pressures Using Static Compression Techniques, Crystals 11 (2021) 416.

[51] S. Anzellini, A. Kleppe, D. Daisenberger, M. Wharmby, R. Giampaoli, S. Boccato, M. Baron, F. Miozzi, D. Keeble, A. Ross, S. Gurney, J. Thompson, G. Knap, M. Booth, L. Hudson, D. Hawkins, M. Walter, H. Wilhelm, Laser-heating system for high-pressure x-ray diffraction at the extreme condition beamline i15 at diamond light source, Journal of Synchrotron Radiation 25 (2018).

[52] C. Prescher, V. Prakapenka, Dioptas: a program for reduction of two-dimensional x-ray diffraction data and data exploration, High Pressure Research 35 (2015) 223.

[53] A. Dewaele, A. B. Belonoshko, G. Garbarino, F. Occelli, P. Bouvier, M. Hanfland, M. Mezouar, High-pressure-high-temperature equation of state of KCl and KBr, Physical Review B - Condensed Matter and Materials Physics 85 (21) (2012) 1–7. doi:10.1103/PhysRevB.85.214105.

[54] L. Benedetti, P. Loubeyre, Temperature gradients, wavelength-dependent emissivity, and accuracy of high and very-high temperatures measured in the laser-heated diamond cell, High Pressure Research 24 (4) (2004) 423–445.

[55] A. Coelho, Topas and topas-academic: an optimization program integrating computer algebra and crystallographic object written in c++, Journal of Applied Crystallography 51 (2018) 210.

[56] P. Blöchl, Projector augmented-wave method, Physical Review B 50 (1994) 17953.

[57] J. P. Perdew, K. Burke, M. Ernzerhof, Generalized gradient approximation made simple, Phys. Rev. Lett. 77 (1996) 3865–3868.

[58] J. Chen, D. Singh, H. Krakauer, Local-density description of antiferromagnetic cr, 1988.

[59] E. Fawcett, Spin-density-wave antiferromagnetism in chromium, Tech. Rep. 272 (1988).

[60] C. Wang, B. Klein, H. Krakauer, Theory of magnetic and structural ordering in iron, 1985.

[61] G. Guo, H. Ebert, W. Temmerman, K. Schwarz, P. Blaha, Relativistic effects on the structural and magnetic properties of iron, Solid State Communications 79 (2) (1991) 121.

[62] P. Bagno, O. Jepsen, O. Gunnarsson, M. Plan-Ck, I.-I. Fiir Festkorperforschung, Postfach, Stuttgart, W. Germany, Ground-state properties of third-row elements with nonlocal density functionals, 1989.

[63] B. Barbiellini, E. Moroni, T. Jarlborg, Effects of gradient corrections on electronic structure in metals, J. Phys.: Condens. Matter 2 (1990) 7597.

[64] D. Hobbs, G. Kresse, J. Hafner, Fully unconstrained noncollinear magnetism within the projector augmented-wave method, Physical Review B 62 (2000) 11556.

[65] L. Burakovsky, N. Burakovsky, D. Preston, Ab initio melting curve of osmium, Physical Review B 92 (2015) 174105.

[66] I. Abrikosov, A. Ponomareva, P. Steneteg, S. Barannikova, B. Alling, Recent progress in simulations of the paramagnetic state of magnetic materials, Current Opinion in Solid State and Materials Science 20 (2) (2016) 85–106. doi:10.1016/j.cossms.2015.07.003.

[67] S. Dudarev, G. Botton, S. Savrasov, C. Humphreys, A. Sutton, Electron-energy-loss spectra and the structural stability of nickel oxide: An lsda-u study, Physical Review B 57 (3) (1998) 1505.

[68] F. Aryasetiawan, K. Karlsson, O. Jepsen, U. Schönberger, Calculation of hubbard u from first-principles, Physical Review B 74 (12) (2006) 125106. doi:10.1103/physrevb.74.125106.

[69] Q. Guo, H.-K. Mao, J. Hu, J. Shu, R. Hemley, The phase transitions of coo under static pressure to 104 gpa, 2002.

[70] S. Nagakura, Study of metallic carbides by electron diffraction part iv. cobalt carbides, Journal of the Physical Society of Japan 16 (6) (1961) 1213.

[71] S. Anzellini, V. Monteseguro, E. Bandiello, A. Dewaele, L. Burakovsky, D. Errandonea, In situ characterization of the high pressure- high temperature meltig curve of platinum, Scientific Reports 9 (2019) 13034.

[72] S. Anzellini, Phase diagram of iron under extreme conditions measured with time-resolved methods, Ph.D. thesis, Université Pierre et Marie Curie (2014).

[73] R. Torchio, S. Boccato, V. Cerantola, G. Morard, T. Irifune, I. Kantor, Probing the local, electronic and magnetic structure of matter under extreme conditions of temperature and pressure, High Press. Res. 36 (3) (2016) 293–302.

[74] R. Briggs, D. Daisenberger, O. T. Lord, A. Salamat, E. Bailey, M. J. Walter, P. F. McMillan, High-pressure melting behavior of tin up to 105 gpa, Phys. Rev. B 95 (2017) 054102.

[75] S. Anzellini, D. Errandonea, S. MacLeod, P. Botella, D. Daisenberger, J. DeAth, J.Gonzalez-Platas, J. Ibanez, M. McMahon, K. Munro, C. Popescu, J. Ruiz-Fuertes, C. W. Wilson, Phase diagram of calcium at high pressure and high temperature, Physical Review Materials 2 (2018) 083608.

[76] A. Dewaele, M. Mezouar, N. Guignot, P. Loubeyre, High melting points of tantalum in a laser-heated diamond anvil cell, Physical Review Letters 104 (25) (2010) 29–31.

[77] A. Dewaele, M. Mezouar, N. Guignot, P. Loubeyre, Melting of lead under high pressure studied using second-scale time-resolved x-ray diffraction, Physical Review B - Condensed Matter and Materials Physics 76 (14) (2007) 1–5. doi:10.1103/PhysRevB.76.144106.

[78] R. J. Angel, J. Gonzalez-platas, M. Alvaro, EosFit7c and a Fortran module (library) for equation of state calculations, Z. Kristallogr. 229 (2014) 405–419.

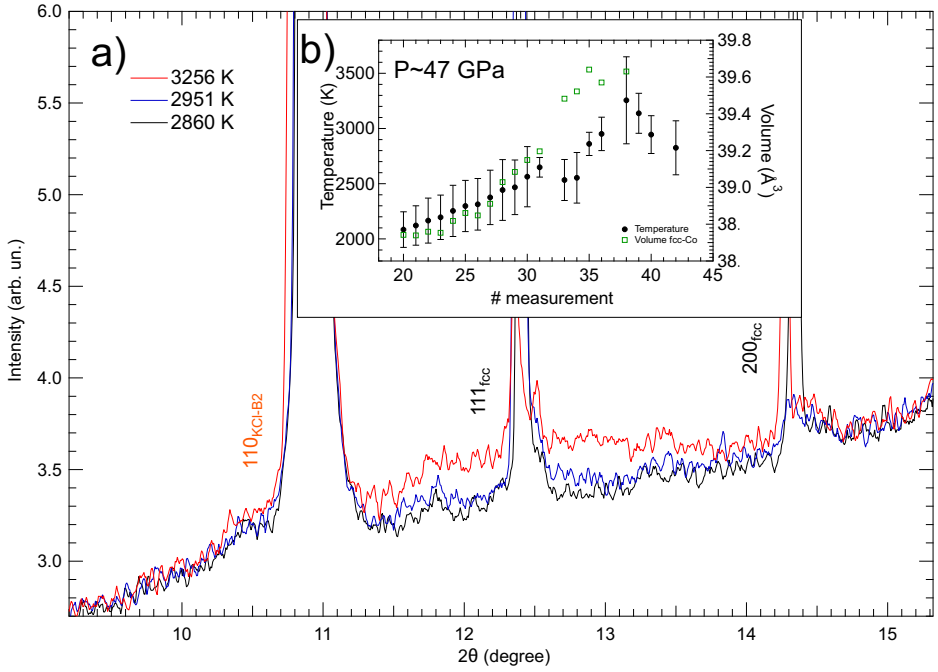

Figure 2: a) Integrated XRD patterns for increasing T around 47 GPa. The onset of melting, characterized by the first appearance of the diffuse signal, is observed at 2951 K (blue pattern). The diffuse scattering increases with the rising T, showing its maximum at 3256 K (red pattern). b) Evolution of T (black points) and sample's volume (green empty points) during the heating ramp performed at 47 GPa. It is possible to observe a plateau in the volumetric expansion starting between the measurement at 2860 K and 2951 K, independently confirming the onset of melting. Concerning the T evolution, it is possible to observe a first plateau after 2500 K ascribed for this particular ramp to the onset of fast re-crystallization. A sudden drop is observed after 3200 K, once the sample is already molten.

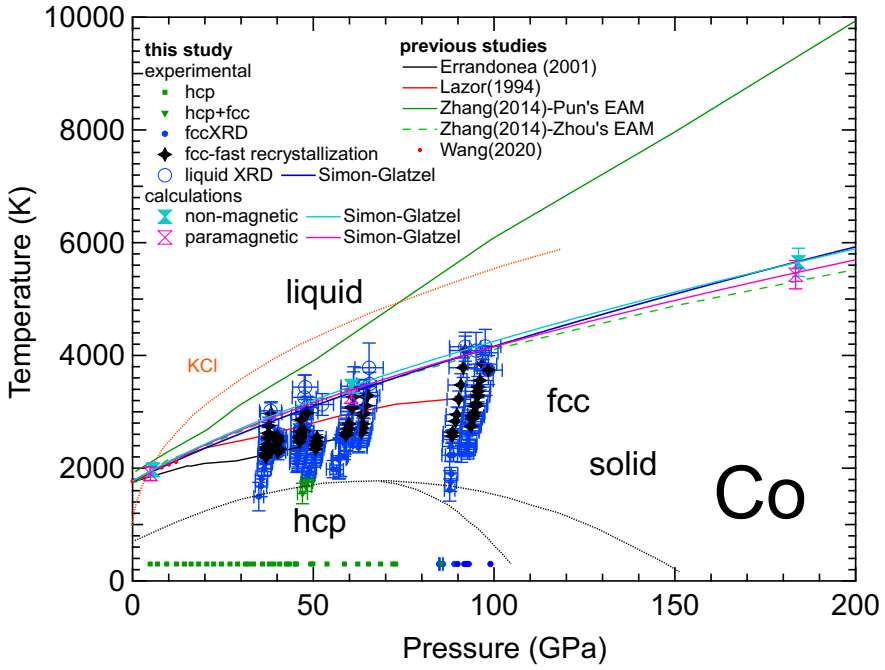

Figure 3: Phase diagram of Co as obtained in the present work compared to literature studies. The solid-solid phase boundary reported as black dashed lines are after Yoo *et al.*(30) and used here as reference. Experimentally observed solid phases are reported as solid points: in green the *hcp* phase(or *hcp*-fcc coexistence), in blue the fcc phase. The empty blue symbols correspond to the experimentally observed liquid points. Black solid diamonds are used to evidence where fast re-crystallization was detected. The melting points calculated in a P-range up to 200 GPa (and their corresponding Simon-Glatzel curves) are reported for both PM and NM fcc-Co for comparison with the present experimental points. For reference, the melting line of KCl is also reported as a dashed orange line.

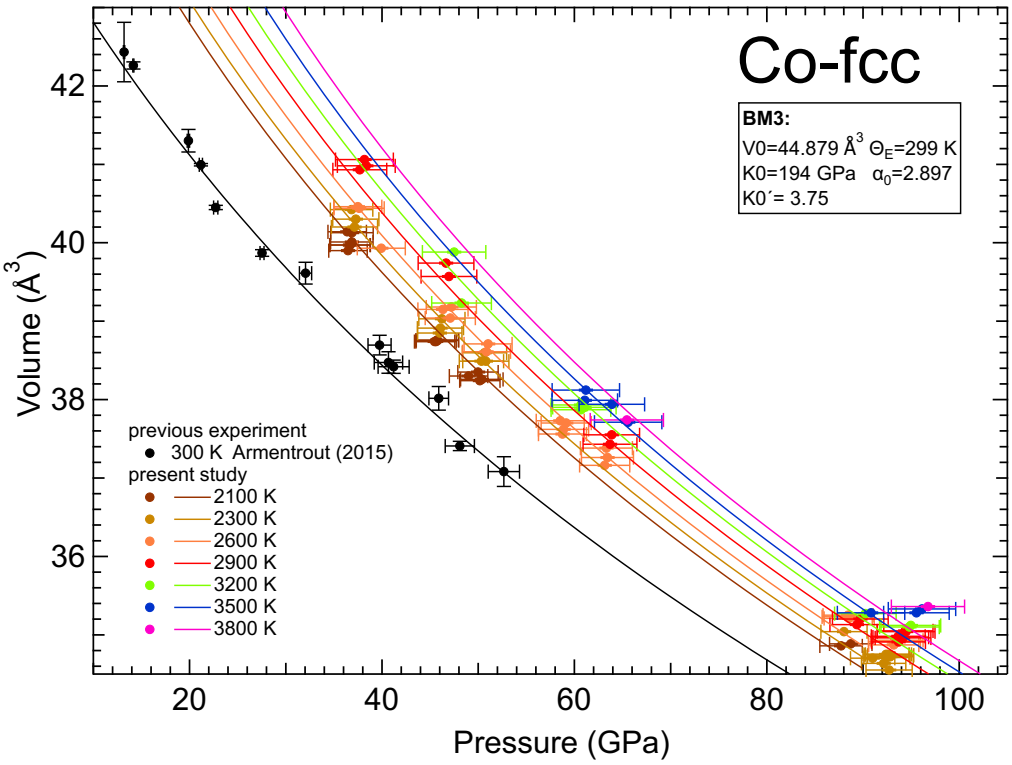

Figure 4: Compression curves of fcc-Co along different isotherms.Temperatures are color-coded as in the legend. The solid lines are the isothermal compression curves calculated according to the thermal equation of state established in the present study